Spatiotemporal Transition to Conduction Block in Canine Ventricle

Jeffrey J. Fox, Mark L. Riccio, Fei Hua, Eberhard Bodenschatz and Robert F. Gilmour, Jr

Circ Res. 2002;90:289-296; originally published online January 10, 2002;
doi: 10.1161/hh0302.104723
Circulation Research is published by the American Heart Association, 7272 Greenville Avenue, Dallas, TX 75231

Print ISSN: 0009-7330. Online ISSN: 1524-4571

Spatiotemporal Transition to Conduction Block in Canine Ventricle

Jeffrey J. Fox, Mark L. Riccio, Fei Hua, Eberhard Bodenschatz, Robert F. Gilmour, Jr

Abstract—Interruption of periodic wave propagation by the nucleation and subsequent disintegration of spiral waves is thought to mediate the transition from normal sinus rhythm to ventricular fibrillation. This sequence of events may be precipitated by a period doubling bifurcation, manifest as a beat-to-beat alternation, or alternans, of cardiac action potential duration and conduction velocity. How alternans causes the local conduction block required for initiation of spiral wave reentry remains unclear, however. In the present study, a mechanism for conduction block was derived from experimental studies in linear strands of cardiac tissue and from computer simulations in ionic and coupled maps models of homogeneous one-dimensional fibers. In both the experiments and the computer models, rapid periodic pacing induced marked spatiotemporal heterogeneity of cellular electrical properties, culminating in paroxysmal conduction block. These behaviors resulted from a nonuniform distribution of action potential duration alternans, secondary to alternans of conduction velocity. This link between period doubling bifurcations of cellular electrical properties and conduction block may provide a generic mechanism for the onset of tachycardia and fibrillation. **(*Circ Res*. 2002;90: 289-296.)**

Key Words: ventricular fibrillation ■ alternans ■ conduction block

Our current understanding of the mechanism for ventricular fibrillation is incomplete, as reflected by the statistic that sudden death continues to be the leading cause of mortality in the Western world. One candidate mechanism for fibrillation is the nucleation of a pair of counterrotating spiral waves, which subsequently disintegrate into multiple wavelets,[1,2] in association with a period doubling bifurcation of cellular electrical properties.[3–6] However, the mechanism by which a period doubling bifurcation may precipitate the local conduction block necessary for the initiation of spiral wave reentry is unknown.

Previous studies have shown that the induction and propagation of period doubling bifurcations in cardiac tissue depend on the recovery properties for action potential duration (D) and conduction velocity (V), where D or V for a given action potential (D_{n+1} or V_{n+1}, respectively) is a function of the preceding interval (I_n) between action potentials.[7–10] If the function $D_{n+1}=f(I_n)$ has a maximum slope ≥ 1, 1:1 stimulus:response locking during pacing at long cycle lengths is replaced by 2:2 locking at short cycle lengths, with 2:2 locking being characterized by beat-to-beat, long-short alternations of D and I.

During 2:2 locking, alternation of I also causes an alternation of V, where $V_{n+1}=c(I_n)$. Alternation of V influences action potential propagation and the spatial distribution of D along a cardiac fiber.[11,12] If the fiber is sufficiently long, the long-short D pattern at one end of the fiber reverses phase and becomes a short-long pattern at the other end. This phenomenon, known as discordant alternans, has been observed in computer simulations of homogeneous one-dimensional cables[11,12] and in experimental studies in isolated hearts.[13,14] However, in the experimental studies, discordant alternans was attributed to intrinsic heterogeneity of cellular electrical properties, with little or no role assigned to dynamical heterogeneity or to conduction velocity alternans.[13,14]

The objectives of the present study were to determine whether dynamical heterogeneity is sufficient for the induction of discordant alternans and conduction block. Studies were conducted in unbranched Purkinje fibers, to approximate as closely as possible a homogeneous linear strand of cardiac tissue, and in ionic and coupled maps models of homogeneous one-dimensional fibers. After verifying that the experimental results and the results generated by the ionic and coupled maps models were in agreement, the coupled maps model was used to identify the dynamical mechanism for the spatiotemporal transition to conduction block.

Materials and Methods

Purkinje Fiber Experiments

Adult dogs of either sex weighing 10 to 30 kg were anesthetized with Fatal-Plus (390 mg/mL pentobarbital sodium; Vortex Pharmaceuticals; 86 mg/kg IV) and their hearts were excised rapidly.[15] Free-

Original received August 23, 2001; resubmission received October 16, 2001; revised resubmission received December 21, 2001; accepted December 21, 2001.

From the Departments of Biomedical Sciences (J.J.F., M.L.R., F.H., R.F.G.) and Physics (J.J.F., E.B.), Cornell University, Ithaca, NY.

Correspondence to Robert F. Gilmour, Jr, Department of Biomedical Sciences, T7 012C VRT, Cornell University, Ithaca, NY 14853-6401. E-mail rfg2@cornell.edu

Circulation Research **is available at http://www.circresaha.org** **DOI: 10.1161/hh0302.104723**

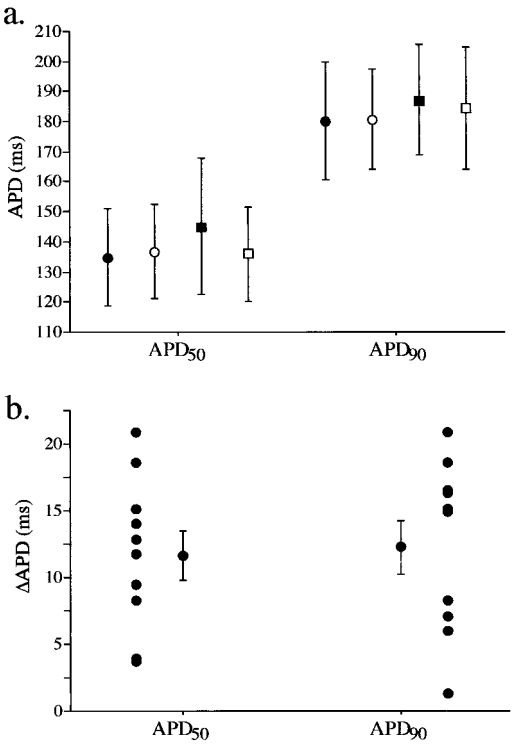

Figure 1. Dispersion of action potential duration, as measured at 50% and 90% of repolarization (APD_{50} and APD_{90}, respectively), in a canine Purkinje fiber during pacing at τ=400 ms. a, Mean (±SE, n=10) APD_{50} and APD_{90} for each of the 4 recording sites, represented by different symbols from left (site 1) to right (site 4). There were no significant differences between the 4 sites. b, Difference between the longest and shortest APD_{50} and APD_{90} (ΔAPD) from the 4 recording sites. Data are shown for each of the 10 fibers (individual points), as well as the mean (±SE) differences.

running unbranched Purkinje fibers (n=10), 13 to 24 mm in length and 1 to 2 mm in width, were excised from either ventricle, mounted in a Plexiglas chamber and superfused with Tyrode's solution at 15 mL/min. The Tyrode's solution was bubbled with 95% O_2 and 5% CO_2. The Po_2 was 400 to 600 mm Hg, the pH was 7.35±0.05, and the temperature was 37.0±0.5°C. The composition of the Tyrode's (in mmol/L) was $MgCl_2$ 0.5, NaH_2PO_4 0.9, $CaCl_2$ 2.0, NaCl 137.0, $NaHCO_3$ 24.0, KCl 4.0, and glucose 5.5. The fibers were stimulated using rectangular pulses of 2 ms in duration and 2 to 3 times the diastolic threshold (0.1 to 0.3 mA), delivered through Teflon-coated bipolar silver electrodes. Transmembrane action potentials recordings were obtained simultaneously from 3 to 4 sites along the fiber using glass capillary electrodes filled with 3 mol/L KCl. The recordings were sampled at 2000 Hz with 12-bit resolution using custom-written data acquisition programs. Online data display and offline data analysis were performed using programs written in Matlab 4.2c run on an Apple Macintosh PowerPC. All experiments were approved by the Institutional Animal Care and Use Committee of the Center for Research Animal Resources at Cornell University. Animals were obtained from a colony of dogs maintained by Cornell University.

One-Dimensional Ionic Models

Cellular action potentials and wave propagation were simulated using a modified version of the Winslow ionic model,[16] as described in detail elsewhere.[17] The model is based largely on data obtained from canine mid-myocardial myocytes (M cells). Briefly, compared with the native Winslow model, I_{K1} was decreased at depolarized potentials, to agree with Freeman et al.[18] The maximum conductance and rectification of I_{Kr} were increased and activation kinetics were slowed, to agree with Gintant.[19] I_{Ks} was increased in magnitude and activation shifted to less positive voltages, to agree with Varro et al.[20] L-type calcium current was modified to produce a smaller, more rapidly inactivating current. Finally, a simplified form of intracellular calcium dynamics was adapted from Chudin et al.[21]

The partial differential equation for a one-dimensional piece of tissue was solved numerically, as described by Qu et al.[22] The length of the one-dimensional cable was set to 220 cells (30 cells longer than the minimum length required for the development of at least one node), with the length of each cell as 200 μm and a diffusion coefficient of 0.001 cm^2/ms.

One-Dimensional Coupled Maps Model

The key determinants of the spatiotemporal dynamics observed experimentally and in the computer simulations were studied in more detail using a coupled maps model of a one-dimensional cardiac fiber.[3,23,24] See the Appendix for details of the model. The defining equation for the model was a summation over space and a difference equation in time:

$$(1)\quad I_{n+1}(x_i)=T_{n+1}(x_i)-D_{n+1}(x_i)$$

$$=\tau+\sum_{j=0}^{i}\frac{\Delta x}{c[I_{n+1}(x_j)]}-\sum_{j=0}^{i}\frac{\Delta x}{c[I_n(x_j)]}-D_{n+1}(x_i)$$

τ was the period delivered to the pacing site and Δx was the length of a single cell. $T_{n+1}(x_i)$, the period between activations $n+1$ and $n+2$, was determined by including the time delays required for an action potential to propagate from the pacing site to site x_i. Conduction velocity $V_{n+1}(x_i)$ depended only on the diastolic interval I through the function $V_{n+1}=c(I_n)$. Action potential duration $D_{n+1}(x_i)$ depended on the diastolic interval I through the function $D_{n+1}=f(I_n)$.

An expanded Materials and Methods section can be found in the online data supplement available at http://www.circresaha.org.

Results

Purkinje Fiber Experiments

To determine whether discordant alternans could be induced in homogenous cable-like cardiac tissue, 10 Purkinje fibers were stimulated at one end at progressively shorter τ and action potentials were recorded along the length of the fiber. The electrophysiological properties of cells at the four recording sites were similar, as shown in Figure 1. Although action potential duration varied between preparations, there was no significant difference in action potential duration at 50% and 90% of repolarization (APD_{50} and APD_{90}, respectively) across the four recording sites (Figure 1a), indicating that within a given preparation, action potential duration was relatively uniform.

To further characterize the ranges of action potential duration, the differences between the longest and shortest action potentials during pacing at a cycle length of 400 ms were calculated for each fiber. As shown in Figure 1b, the difference in action potential duration was less than 22 ms for all preparations, with a mean difference of 11.6±1.8 ms for APD_{50} and 12.3±2.0 ms for APD_{90} (mean±SE). Resting membrane potential and action potential amplitude also were similar within a given fiber, with maximum differences of 2.1±0.5 mV and 3.2±0.7 mV (mean±SE), respectively, and no significant differences across the four recording sites (data not shown).

Pacing the fibers at τ=120 to 220 ms induced concordant D alternans, whereas pacing at shorter τ induced discordant D alternans (Figure 2a). The latter progressed to 2:1 conduction

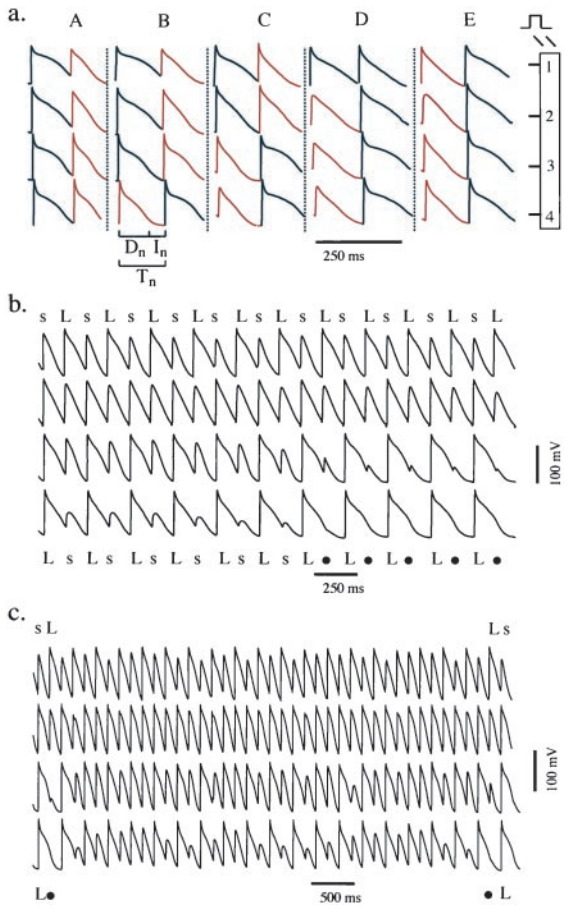

Figure 2. Spatially distributed action potential dynamics in a canine cardiac Purkinje fiber. a, Pairs of action potentials recorded from 4 cells (see diagram, right; length=22 mm) during pacing at τ=100 ms. The shorter-duration action potentials are shown in red. Over time, concordant *D* alternans (A) was replaced progressively by discordant *D* alternans; first, site 4 became discordant (B), then site 3 (C) and then site 2 (D). Note that as site 4 became discordant, the action potential durations at site 3 changed from long-short (2:2) to intermediate-intermediate (1:1), representing the transition zone, or node, between regions of long-short *D* and short-long *D*. Eventually the node migrated to site 1 and concordant *D* alternans was restored temporarily (E), until a new node formed at site 4 (note reduction in *D* alternans magnitude between panels D and E, reflecting the transition from 2:2 to 1:1) and the evolution of discordant alternans was repeated (not shown). b, Development of 2:1 conduction block at τ=120 ms, where L and s are long and short *D*, respectively, and ● indicates conduction block. Note discordant alternans (L-s at 1 and s-L at 4) before the development of block. c, Transient recovery from 2:1 block at τ=120 ms. During 2:1 block, L and s *D* at site 1 correspond to block (●) and L, respectively, at site 4 (left), a pattern that recurs after restoration of block (right).

block at the distal recording site (Figure 2b). In 5 of the 10 fibers, the 2:1 conduction block was paroxysmal: over time during pacing at the same τ, a pattern of 2:1→2:2→2:1 locking occurred (Figure 2c). In the remaining 5 fibers, 2:1 conduction block was stable (nonparoxysmal) and was limited to the 2 distal recording sites in 3 fibers and migrated to the site of stimulation in 2 fibers (Figure 3).

Conduction block always developed initially at the distal end of the fiber and never in the absence of discordant alternans. Moreover, the same sequence of dynamics occurred regardless of which end of the fiber was paced, attesting to the homogeneity of intrinsic cellular electrical properties in the preparations.

One-Dimensional Ionic Model

Rapid pacing also induced concordant and discordant *D* alternans and paroxysmal 2:1 conduction block in computer simulations of homogeneous one-dimensional fibers (see Figure 4 and online movies). Unlike in the experiments, it was possible in the simulations to monitor action potentials from each cell on the fiber and thereby demonstrate the spatially distributed transition from concordant *D* alternans to discordant *D* alternans and paroxysmal 2:1 conduction block. As shown in Figure 4, at longer cycle lengths (eg, 177 ms; Figures 4a through 4c) the node migrated slowly through the fiber, leaving in its wake discordant *D* alternans (Figure 4b) and 2:1 block (Figure 4c). At a shorter cycle length (170 ms; Figure 4d), the node migrated more rapidly, eventually reaching the site of stimulation. Shortly thereafter, conduction was restored transiently throughout the fiber, until a new node developed and migrated to a point on the fiber where 2:1 block resumed. This sequence of events was then repeated.

In agreement with our previous studies in a single myocyte model,[17] both concordant and discordant *D* alternans along the one-dimensional fiber were associated with alternans of peak I_{Ca}, whereas at the node, *D* and I_{Ca} were constant (Figure 5). Alternation of other ionic currents also accompanied *D* alternans, but alternations of these currents appeared to result from the *D* alternans, rather than being the underlying mechanism for them. For example, peak I_{Kr} alternated during *D* alternans, yet the larger peak was associated with the longer action potential, contrary to what would be expected if

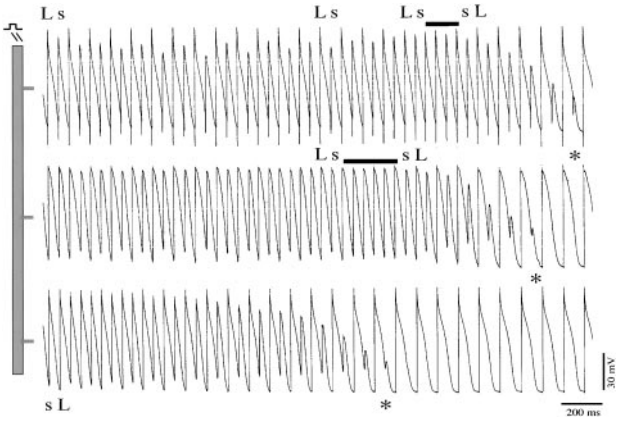

Figure 3. Spatially distributed action potential dynamics in a canine cardiac Purkinje fiber. Action potentials were recorded from 3 cells along the fiber (see diagram, left; length=24 mm) during pacing at τ=100 ms. At the beginning of the record, alternans of *D* is discordant (L-s at site 1 versus s-L at site 3). Over time, 2:1 conduction block occurs at site 3 (indicated by the asterisk). The development of 2:1 conduction block at site 3 is associated with migration of the node through site 2, as reflected by the transition from L-s pairs of *D* to s-L pairs (indicated by the bar). Subsequently, 2:1 conduction block occurs at site 2, which is, in turn, associated with migration of the node through site 1 (L-s converts to s-L, as indicated by the bar). Migration of the node to site 1 is followed shortly thereafter by 2:1 conduction block.

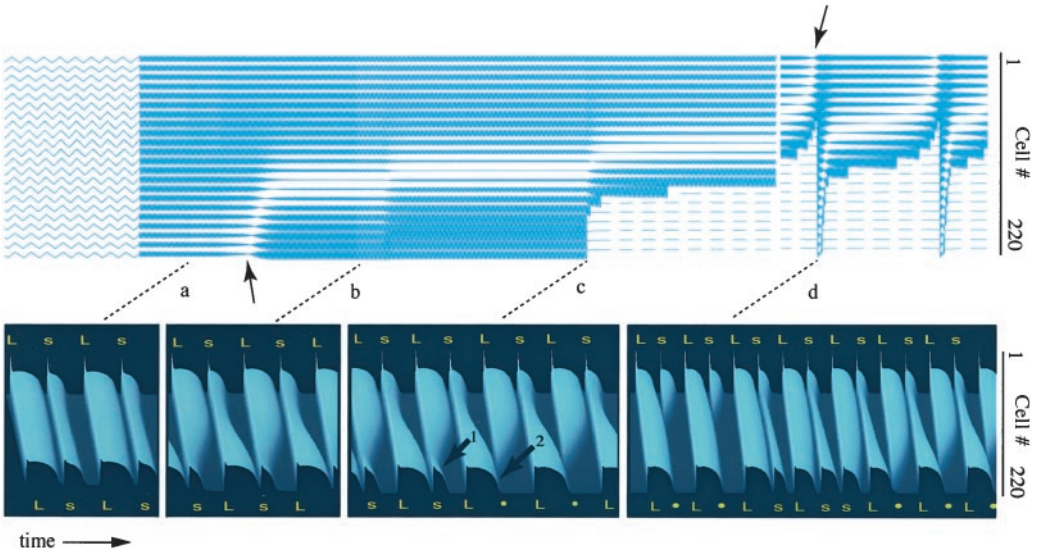

Figure 4. Spatially distributed action potential dynamics in a one-dimensional ionic model. Top, *D* time series measured from 22 cells during propagation from the pacing site (cell 1) to the end of the fiber (cell 220). The amplitude of the sawtooth *D* pattern indicates the magnitude of *D* alternans (see segment of the record shown at an expanded time scale, left). At τ=177 ms, concordant *D* alternans (a) converted to discordant *D* alternans (b), with the transition between behaviors marked by the development of a node (arrow on the left side). Over time, the node migrated to cell 1 (arrow on the right side). Reducing τ to 175 ms (c) induced 2:1 conduction block at the distal end of the fiber (indicated by broken lines). A further reduction of τ to 170 ms (at the gap in the record) induced repeating episodes of transient recovery from block (d). Bottom, Snapshots of selected dynamics illustrated using action potentials recorded from all 220 cells. a, Concordant *D* alternans, where long (L) and short (s) *D* at cell 1 correspond to L and s *D* at cell 220. b, Discordant *D* alternans, where L and s *D* at cell 1 correspond to s and L *D*, respectively, at cell 220. c, Development of 2:1 conduction block. During discordant *D* alternans, the rapidly conducting action potential with long *D* became shorter and conducted more slowly as it encroached on the previous action potential (arrow 1). 2:1 block (L followed by ●) occurred when the long action potential encountered a rest interval too short to allow conduction (arrow 2). d, Transient recovery from 2:1 block. This figure contains snapshots from the following movies found in the online data supplement, available at http://www.circresaha.org. Ionic Movie A: Concordant alternans (Figure 4a) and the transition to discordant alternans (Figure 4b). Ionic Move B: Discordant alternans and the start of conduction block in the distal region (Figure 4c). Ionic Movie C: Paroxysmal conduction block (Figure 4d).

I_{Kr} were the primary determinant of *D* during alternans (Figure 5).

Reduction of I_{Ca} or elevation of I_{Kr} eliminated electrical alternans at the site of stimulation, as expected from our results using the single myocyte model.[17] In the absence of *D* alternans at the site of pacing, rapid pacing did not induce *D* alternans at other sites on the fiber or a transition to conduction block along the fiber (Figure 6). Instead, 1:1 locking eventually was replaced by stable 2:1 conduction block at all sites (not shown). The link between *D* alternans at the site of stimulation and the transition to discordant alternans and conduction block is described in detail in the next section.

One-Dimensional Coupled Maps Model

Iteration of the coupled maps model (Equation 1) produced a spatial distribution of $D_n(x_i)$ and $T_n(x_i)$ (Figure 7 and online movie) similar to that observed experimentally and in the ionic model. The mechanism for the spatial distribution of *D* and *T* is given in Figure 7, which shows iterations of the return map at a different *T*. During concordant *D* alternans, *D* alternans magnitude decreased and local *T* alternans magnitude increased from the proximal to distal ends of the fiber (Figure 7a). Local *T* alternans grew because differences in conduction delays increased with increasing distance from the pacing site. During concordant *D* alternans, the long action potential iterated to a long *T*, causing a contraction in the magnitude of *D* alternans (compare Figures 8b and 8c).

For sufficiently large *T* alternans, concordant *D* alternans became unstable and converted to discordant *D* alternans (Figures 7b and 7c). If I_1 and I_2 are the two intervals during alternans, this instability occurred when the product of the slopes of the recovery function at those *I*s was $\geq$1 [ie, $|f'(I_1)f'(I_2)|\geq 1$, where $D=f(I)$]. Discordant *D* alternans had a larger magnitude because the pattern of iteration switched, becoming long *D* to short *T* (Figure 8d). During discordant *D* alternans, the transition point (node) between regions of short-long and long-short *D* migrated over time toward the pacing site. As pacing continued, several nodes accumulated in the fiber, leading to significant dynamic heterogeneity of *D* (Figures 7d and 7e).

Paroxysmal 2:1 block (Figure 7f) occurred when the magnitude of *D* and *T* alternans distal to the node became so large that attempted activation at short *T* failed (Figure 8e). As the node continued to migrate toward the pacing site, the magnitude of *T* alternans decreased (became closer to τ) and recovery from 2:1 block occurred (Figures 7g and 7h and Figure 8f). As new nodes formed and migrated, this process was repeated. Thus, for any given activation of the cable during sufficiently rapid pacing, regions of long *D*, short *D*, and conduction block coexisted, as in the experiments.

Although changes in the magnitude of *T* alternans were required for the transitions from concordant to discordant alternans and for the subsequent transition to paroxysmal 2:1 block, the magnitude of *T* alternans was small, compared with

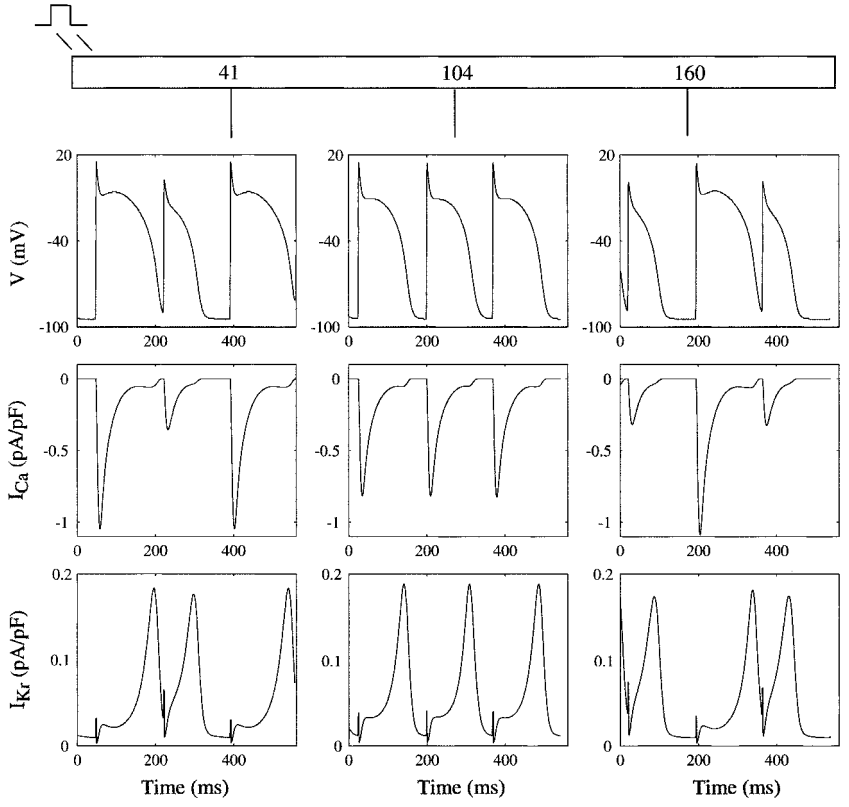

Figure 5. Ionic mechanism for electrical alternans and the transition to conduction block in a one-dimensional ionic model. Recordings of action potentials (top), I_{Ca} (middle), and I_{Kr} (bottom) are shown for 3 consecutive activations at 3 sites on the fiber (cells 41, 104, and 160; see diagram, top) during pacing at τ=170 ms. The 3 recording sites were selected to illustrate the behavior at the node (site 104) and at two sites having approximately the same magnitude of *D* alternans during discordant alternans (ie, long-short *D* sequence at site 41 and short-long *D* sequence at site 160).

the magnitude of *D* alternans (Figure 7). At the onset of discordant alternans, ΔT was only $\pm$0.9 ms (Figure 7c), increasing to $\pm$4.6 ms at the onset of 2:1 block (Figure 7f) and decreasing to approximately $\pm$2.1 ms at the resumption of 2:2 locking (Figure 7h). The corresponding values for the experimental data were similar ($\pm$1.0, $\pm$1.6, and $\pm$1.2 ms, respectively), as were the values for the ionic model ($\pm$4.0, $\pm$3.0, and $\pm$2.0 ms, respectively). Note that the maximum beat-to-beat differences in *T* occurred in a region of the fibers where the magnitude of *D* alternans was minimal (Figure 7). Conversely, the minimum values of ΔT occurred where *D* alternans magnitude was maximal (Figure 7).

Discussion

Spatially Distributed Complex Dynamics

The spatial distribution of complex dynamics observed in the present study depended on three key cellular electrical properties. The first was a *D* recovery function with slope $\geq$1, without which *D* alternans would not have occurred at the

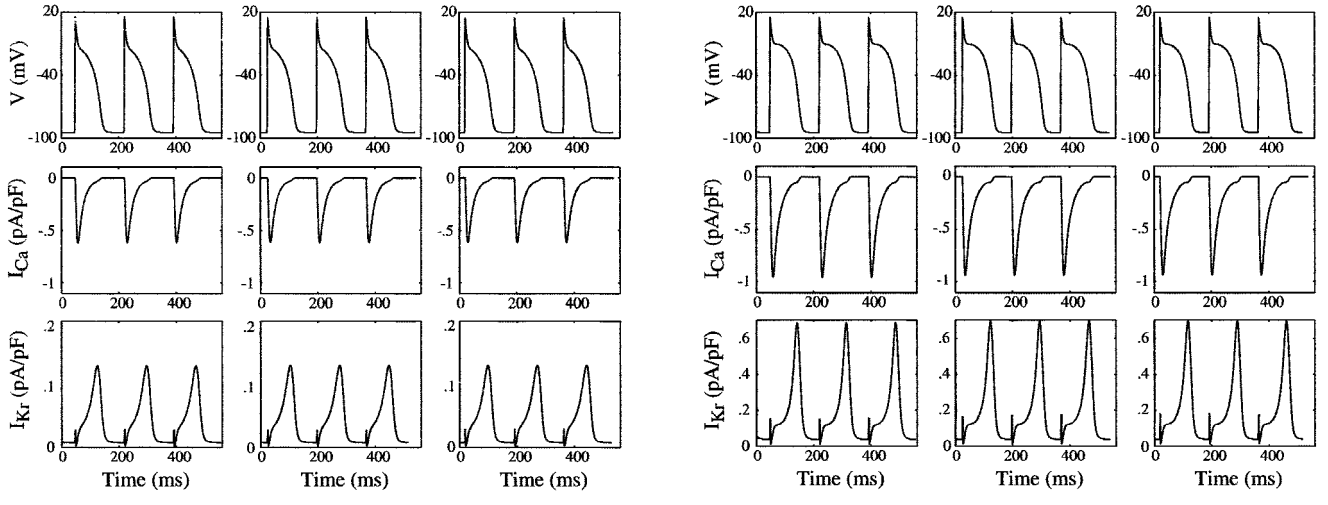

Figure 6. Suppression of concordant and discordant *D* alternans produced by decreasing the magnitude of I_{Ca} (left panels) or increasing the magnitude of I_{Kr} (right panels). Same format as in Figure 5. Reduction of I_{Ca} (by decreasing pCa from $0.226e^{-4}$ to $0.113e^{-4}$) abolished alternans at the site of stimulation and at all sites along the fiber at all τ (τ=170 ms shown). Increasing I_{Kr} (by increasing GbarKr from 0.0136 to 0.0544) had a similar suppressant effect on alternans.

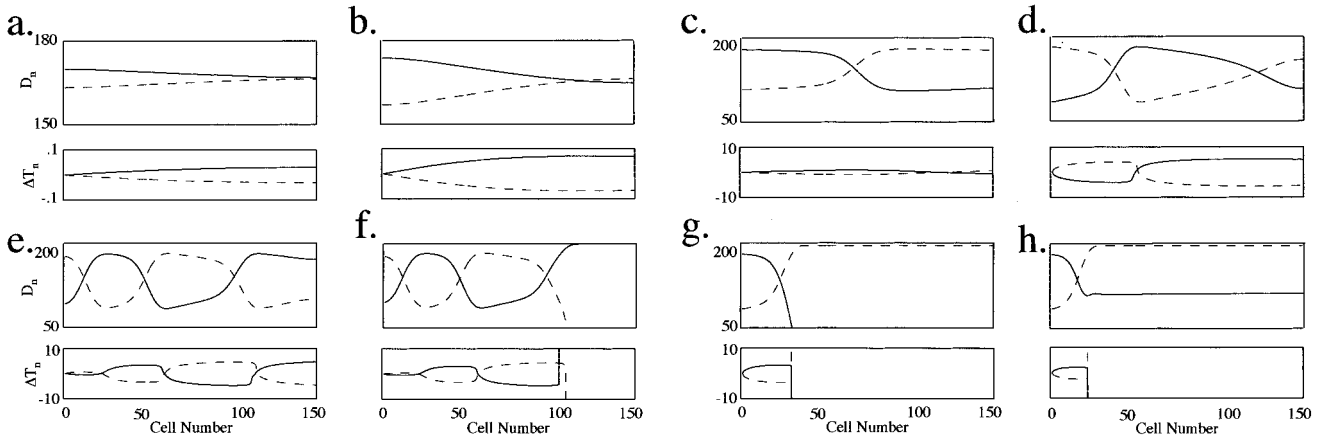

Figure 7. D_n and ΔT_n ($T_n-\tau$) versus cell number in the coupled maps model for two consecutive beats (dashed line, beat n; solid line, beat $n+1$) during simulation at progressively shorter τ. All time units are in ms and all space units are in mm. Stimuli were delivered to the first cell and activation propagated along the fiber. τ=232 ms in a, 230 ms in b, 220 ms in c, and 202 ms in panels d through h. a, Concordant *D* alternans. b, Development of discordant *D* alternans at the distal end of the fiber with increasing beat-to-beat differences in *T*. c, Discordant *D* alternans with a single node. d, Discordant *D* alternans with two *D* nodes. Note that *D* nodes corresponded to maxima (antinodes) in *T* differences, and *D* antinodes corresponded to *T* nodes. e, Time-dependent migration of existing nodes toward the pacing site and the formation of new nodes at the distal end of the fiber. f, 2:1 conduction block. g, Time-dependent migration of the boundary between normal conduction and 2:1 block until the *T* differences at the boundary became small enough to allow conduction (h). This figure contains snapshots from the following movie found in the online data supplement. Coupled Maps Movie: Figure 7a, beats 81 and 82 (concordant alternans); Figure 7b, beats 129 and 130 (development of discordant alternans); Figure 7c, beats 235 and 236 (discordant alternans with one node); Figure 7d, beats 1231 and 1232 (discordant alternans with two nodes); Figure 7e, beats 1285 and 1286 (discordant alternans with three nodes); Figure 7f, beats 1289 and 1290 (2:1 block); Figure 7g, beats 1341 and 1342 (migration of the boundary between normal conduction and 2:1 block); and Figure 7h; beats 1351 and 1352 (recovery of conduction).

pacing site or at any other site on the fiber. The second was the electrotonic interaction between cells, represented by diffusion in the ionic model and by spatial averaging in the coupled maps models. The role of spatial averaging was identified by removing it from the coupled maps model. In the absence of averaging, concordant and discordant alternans and 2:1 conduction block still occurred (not shown). However, paroxysmal 2:1 block did not occur. Rather, conduction block was stable, as were the steady-state positions of the nodes. Without migration of the nodes toward the pacing site, *T* differences remained sufficiently large to sustain block.

The third requirement for the development of complex dynamics was a recovery function for conduction velocity. If *V* were a constant, $D_{n+1}(x_i)$ for any given beat would be the same for each site on the fiber (see Equation 1), precluding the possibility of discordant alternans. However, the magnitude of *V* alternans and the resultant *T* alternans during discordant alternans typically were small (≈2 ms), particularly in the region of largest *D* alternans (Figure 7). *T* alternans of this magnitude is likely to be obscured under most experimental circumstances, which may account for the conclusion reached by Pastore and Rosenbaum that *T* alternans is not required for the induction of discordant *D* alternans,[13,14] whereas intrinsic spatial heterogeneity of action potential duration is. Although our experiments indicate that discordant *D* alternans can be induced in the absence of intrinsic heterogeneity, it seems likely that preexisting gradients of repolarization[13,25,26] may affect the development of discordant *D* alternans.

Implications

The results of these experiments demonstrate for the first time a complete transition from planar wave propagation, through alternans to local conduction block, where the spatiotemporal heterogeneity required for the induction of these phenomena developed dynamically. Of clinical interest is the possibility that the mechanism for conduction block developed in the present study may contribute not only to the initiation of spiral wave reentry but also to the subsequent fractionation of wave propagation associated with stable, meandering, or disintegrating spiral waves.[2,27,28] This idea remains to be tested. But, if it is found to be valid, interrupting the spatiotemporal transition to conduction block may provide a key to prevention of lethal heart rhythm disorders.[5,29]

Appendix

To characterize the determinants of the spatiotemporal dynamics observed experimentally, we used a coupled maps model of a one-dimensional cardiac fiber.[3,23,24] The model is given by the equation:

$$I_{n+1}(x_i)=T_{n+1}(x_i)-D_{n+1}(x_i) \quad (2)$$

$T_{n+1}(x_i)$ equals the period between activations of site x_i. $T_{n+1}(x_i)$ is determined by including the time delays required for an action potential to propagate from the pacing site to site x_i. This yields

$$V_n(x_i)=c[I_n(x_i)] \quad (3)$$

$$T_{n+1}(x_i)=\tau+\sum_{j=0}^{i}\frac{\Delta x}{c[I_{n+1}(x_j)]}-\sum_{j=0}^{i}\frac{\Delta x}{c[I_n(x_j)]}$$

where τ is the period delivered to the pacing site, and Δx is the length of a single cell. The conduction velocity $V_n(x_i)$ depends only on the diastolic interval *I* through the *V* restitution function $V_n=c(I_n)$.

The defining equation for the model is a summation over space and a difference equation in time:

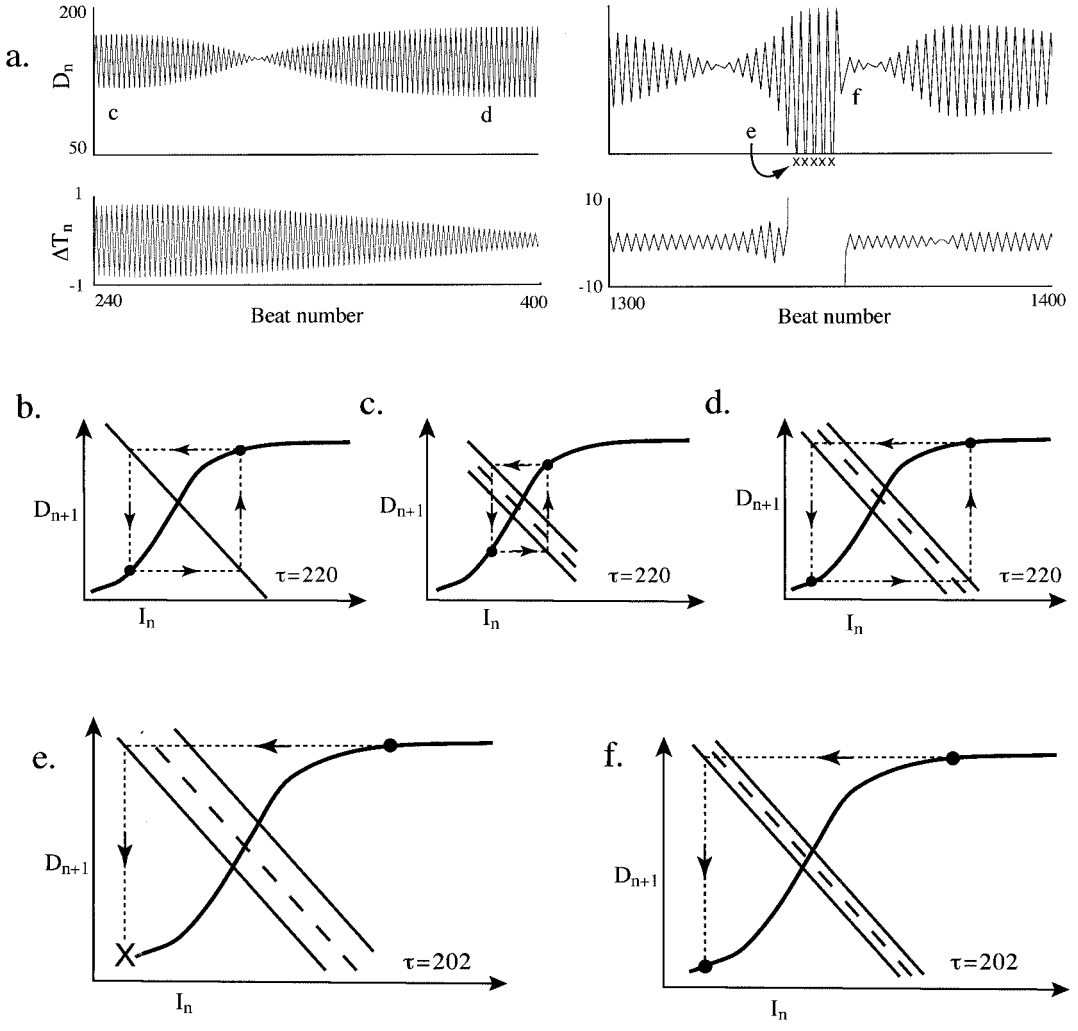

Figure 8. Mechanism for local conduction block. a, D_n and ΔT_n as a function of beat number for a cell distal to the pacing site. b through f, Graphical iteration of the return map $I_n(x_i)=T_n(x_i)-D_n(x_i)$. Because the actual data produce very small changes in the local period T, we use hypothetical curves to schematically illustrate the mechanism. b, Iteration of the map for the first cell in the fiber. The curve is a hypothetical function $D_n=f(I_n)$. The line is the equation $D_n+I_n=\tau$, which in this case is 220 ms. The choice of the period (τ) determines where the line intersects the curve. The map is iterated by starting with some choice of I, then moving up to the curve to find D. The next I is found by moving over to the period line, and the process repeats. In this example, the map iterates to stable alternans. c, Concordant D alternans further out on the fiber. The solid lines are the short and long T that result from beat-to-beat differences in conduction delays during alternans. The dashed line is the pacing τ. Note that the long D iterates to the longer of the two T and vice versa, which decreases the magnitude of D alternans, compared with the first cell in the fiber (a). At some point further out on the fiber, the alternans disappears altogether, which corresponds to the node. d, Discordant D alternans at a cell on the fiber distal to the node. Here the pattern of iteration is reversed, with the long D iterating to the short T and vice versa, which increases the magnitude of D alternans. e, 2:1 conduction block at a location on the fiber distal from the pacing site at τ=202 ms. At the shorter pacing τ, D alternans at the site of stimulation is increased, which increases T alternans at this distal site. The long D now iterates to an I at which no D is available, corresponding to a blocked beat (X). f, Recovery of normal conduction at the distal site. Over time, as the node migrates toward the site of stimulation, the magnitude of D alternans at that site decreases, which decreases the magnitude of T alternans at this distal site (compare Figures 7g and 7h). Iteration of the long D to the short T now yields an I at which a new D is available.

$$(4)\qquad I_{n+1}(x_i)=\tau+\sum_{j=0}^{i}\frac{\Delta x}{c[I_{n+1}(x_j)]}-\sum_{j=0}^{i}\frac{\Delta x}{c[I_n(x_j)]}-D_{n+1}(x_i)$$

The coupled maps model used the following functions and parameters. All time units are in ms and all space units are in mm. The duration of the $n+1^{th}$ action potential is a function of the n^{th} rest interval, with $D_{n+1}=f(I_n)$:

$$(5)\qquad f(I)=\frac{220}{1+e^{\frac{20-I}{40}}}$$

as determined by experimental data.[15] For $I_n<I_{min}=2$ ms, $f(I_n)=0$ (conduction block). The V restitution function $V_n=c(I_n)$ is given by

$$(6)\qquad c(I)=0.5(1.43-1.15e^{-0.075I}+0.67e^{-0.15I}-1.34e^{-0.225I})$$

also determined from experimental data (authors' unpublished data, 2001) and using the fitting function from Karma.[3] Coupling is included by a weighted averaging of $D_{n+1}(x_i)$ over a distance α[24]:

$$(7)\qquad D_{n+1}(x_i)=\sum_{j=-\alpha}^{\alpha}w_j f[I_n(x_{i+j})]$$

$$w_j = \frac{e^{-\mu j^2}}{\sum_{j=-\alpha}^{\alpha} e^{-\mu j^2}}$$

with $\alpha = 50$ and $\mu = 0.06$. We set the length of each cell Δx to 0.1 mm. If the index α falls outside the 150-cell cable, that term is not included in the sums in Equation 7.

Acknowledgments

These studies were supported by NIH grant HL62543 (R.F.G.), by an Integrated Graduate Education and Research Traineeship Program (IGERT) grant from the National Science Foundation (J.J.F.), and by a predoctoral fellowship (F.H.) and grant-in-aid (R.F.G.) from the American Heart Association, New York State Affiliate, Inc. We thank Amanda Werthman for assisting with the data analysis.

References

1. Chen PS, Wolf P, Dixon EG, Danieley ND, Frazier DW, Smith WM, Ideker RE. Mechanism of ventricular vulnerability to single premature stimuli in open chest dogs. *Circ Res*. 1988;62:1191–1209.
2. Witkowski FX, Leon LJ, Penkoske PA, Giles WR, Spano ML, Ditto WL, Winfree AT. Spatiotemporal evolution of ventricular fibrillation. *Nature*. 1998;392:78–82.
3. Karma A. Electrical alternans and spiral wave breakup in cardiac tissue. *Chaos*. 1994;4:461–472.
4. Gilmour RF Jr, Chialvo DR. Editorial. Electrical restitution, critical mass and the riddle of fibrillation. *J Cardiovasc Electrophysiol*. 1999;10:1087–1089.
5. Garfinkel A, Kim Y-H, Voroshilovsky O, Qu Z, Kil JR, Lee M-H, Karagueuzian HS, Weiss JN, Chen P-S. Preventing ventricular fibrillation by flattening cardiac restitution. *Proc Natl Acad Sci U S A*. 2000;97:6061–6066.
6. Panfilov AV. Spiral breakup as a model of ventricular fibrillation. *Chaos*. 1998;8:57–64.
7. Nolasco JB, Dahlen RW. A graphic method for the study of alternation in cardiac action potentials. *J Appl Physiol*. 1968;25:191–196.
8. Guevara MR, Ward G, Shrier A, Glass L. Electrical alternans and period doubling bifurcations. *IEEE Comp Cardiol*. 1984;562:167–170.
9. Chialvo DR., Jalife J. Non-linear dynamics of cardiac excitation and impulse propagation. *Nature*. 1987;330:749–752.
10. Chialvo DR, Gilmour RF Jr, Jalife J. Low dimensional chaos in cardiac tissue. *Nature*. 1990;343:653–657.
11. Qu Z, Garfinkel A, Chen PS, Weiss JN. Mechanisms of discordant alternans and induction of reentry in a simulated cardiac tissue. *Circulation*. 2000;102:1664–1670.
12. Watanabe MA, Fenton FH, Evans SJ, Hastings HM, Karma A. Mechanisms for discordant alternans. *J Cardiovasc Electrophysiol*. 2001;12:196–206.
13. Pastore JM, Girouard SD, Laurita KR, Akar FG, Rosenbaum DS. Mechanism linking T-wave alternans to the genesis of cardiac fibrillation. *Circ Res*. 1999;99:1385–1394.
14. Pastore JM, Rosenbaum DS. Role of structural barriers in the mechanism of alternans-induced reentry. *Circ Res*. 2000;87:1157–1163.
15. Koller ML, Riccio ML, Gilmour RF Jr. Dynamic restitution of action potential duration during electrical alternans and ventricular fibrillation. *Am J Physiol*. 1998;275:H1635–H1642.
16. Winslow RL, Rice J, Jafri S, Marbán E, O'Rourke B. Mechanisms of altered excitation-contraction coupling in canine tachycardia-induced heart failure, II: model studies. *Circ Res*. 1999;84:571–586.
17. Fox JJ, McHarg J, Gilmour RF Jr. Ionic mechanism of electrical alternans. *Am J Physiol*. 2002;282:H516–H530.
18. Freeman LC, Pacioretty LM, Moïse NS, Kass RS, Gilmour RF Jr. Decreased density of I_{to} in left ventricular myocytes from German shepherd dogs with inherited arrhythmias. *J Cardiovasc Electrophysiol*. 1997;8:872–883.
19. Gintant GA. Characterization and functional consequences of delayed rectifier current transient in ventricular repolarization. *Am J Physiol*. 2000;278:H806–H817.
20. Varro A, Balati B, Iost N, Takacs J, Virag L, Lathrop DA, Csaba L, Talosi L, Papp JG. The role of the delayed rectifier component I_{Ks} in dog ventricular muscle and Purkinje fibre repolarization. *J Physiol*. 2000;523(pt 1):67–81.
21. Chudin E, Goldhaber J, Garfinkel A, Weiss J, Kogan B. Intracellular Ca^{2+} dynamics and the stability of ventricular tachycardia. *Biophys J*. 1999;77:2930–2941.
22. Qu Z, Kil J, Xie F, Garfinkel A, Weiss JN. Scroll wave dynamics in a 3D cardiac tissue model: roles of restitution, thickness, and fiber rotation. *Biophys J*. 2000;78:2761–2775.
23. Courtemanche M, Glass L, Keener JP. Instabilities of a propagating pulse in a ring of excitable media. *Phys Rev Lett*. 1993;70:2182–2185.
24. Vinet A. Quasiperiodic circus movement in a loop of cardiac tissue: multistability and low dimensional equivalence. *Ann Biomed Eng*. 2000;28:704–720.
25. Yan GX, Shimizu W, Antzelevitch C. Characteristics and distribution of M cells in arterially perfused canine left ventricular wedge preparations. *Circulation*. 1998;98:1921–1927.
26. Choi BR, Liu T, Salama G. The distribution of refractory periods influences the dynamics of ventricular fibrillation. *Circ Res*. 2001;88:e49–e58.
27. Gray RA, Pertsov AM, Jalife J. Spatial and temporal organization during cardiac fibrillation. *Nature*. 1998;392:75–78.
28. Chen J, Mandapati R, Berenfeld O, Skanes AC, Jalife J. High-frequency periodic sources underlie ventricular fibrillation in the isolated rabbit heart. *Circ Res*. 2000;86:86–93.
29. Riccio ML, Koller ML, Gilmour RF Jr. Electrical restitution and spatiotemporal organization during ventricular fibrillation. *Circ Res*. 1999;84:955–963.

Online Data Supplement

To study the ionic mechanism of electrical alternans in canine myocytes, we constructed a canine ventricular myocyte (CVM) model using appropriate formulations of ionic currents from the LRd[1,2], Winslow[3] and Chudin[4] models, altered as necessary to fit experimental voltage clamp data from canine ventricular myocytes. It has been well established that cellular electrical properties in the canine ventricle vary, both between right and left ventricles and within a given ventricle, according to whether a cell resides in the epicardium, endocardium or mid-myocardium[5,6]. Because the Winslow model is the only existing ionic model based on the electrical properties of canine ventricle, we elected to use that model as the basis for the CVM model. Consequently, the CVM model, like its predecessor, recreates the mid-myocardial or M cell action potential. Further alterations of various currents, including I_{Ks}, I_{to} and I_{NaCa}, would be required to model the electrical activity of canine endocardial and epicardial myocytes[5,7].

The CVM model contains the following ionic current formulations:

$$\frac{dV}{dt} = -(I_{stim} + I_{Na} + I_{K1} + I_{Kr} + I_{Ks} + I_{to} + I_{Kp} + I_{NaK} + I_{NaCa} + I_{Nab} + I_{Cab} + I_{pCa} + I_{Ca} + I_{CaK})$$

I_{stim}

The stimulus current used to drive the model is a square wave pulse consisting of –80 uA/uF of current for 1 ms.

I_{Na}

The sodium current is the same as that used in the Winslow model[3], except that the discontinuities in the h and j gate formulations were removed.

$$I_{Na} = \overline{G}_{Na} m^3 hj(V - E_{Na})$$

$$\frac{dm}{dt} = \alpha_m(1 - m) - \beta_m$$

$$\frac{dh}{dt} = \alpha_h(1 - h) - \beta_h$$

$$\frac{dj}{dt} = \alpha_j(1 - j) - \beta_j$$

$$E_{Na} = \frac{RT}{F}\ln(\frac{[Na^+]_o}{[Na^+]_i})$$

$$\alpha_m = .32\frac{V + 47.13}{1 - e^{-.1(V+47.13)}}$$

$$\beta_m = .08e^{-\frac{V}{11}}$$

$$\alpha_h = .135e^{\frac{(V+80)}{-6.8}}$$

$$\beta_h = \frac{7.5}{1 + e^{-.1(V+11)}}$$

$$\alpha_j = \frac{.175e^{\frac{V+100}{-23}}}{1 + e^{.15(V+79)}}$$

$$\beta_j = \frac{.3}{1 + e^{-.1(V+32)}}$$

I_{K1}

I_{K1} was formulated to agree with data from Freeman *et al*[8]. These data indicate a smaller outward current at depolarized potentials than is seen in the Winslow model.

$$I_{K1} = \overline{G}_{K1} K_1^{\infty}(\frac{[K^+]_o}{[K^+]_o + K_{mK1}})(V - E_K)$$

$$K_1^{\infty} = \frac{1}{2 + e^{1.62\frac{F}{RT}(V - E_K)}}$$

$$E_K = \frac{RT}{F}\ln(\frac{[K^+]_o}{[K^+]_i})$$

I_{Kr}

The rapid delayed rectifier current was fit to the data from Gintant[9]. In particular, we reproduced the voltage clamp experiment used to generate figure 2 in his paper. The Winslow formulation of the current was altered to increase rectification, slow kinetics at depolarized potentials and increase maximum conductance.

$$I_{Kr} = \overline{G}_{Kr} R(V) X_{Kr} \sqrt{\frac{[K^+]_o}{4}} (V - E_K)$$

$$\frac{dX_{Kr}}{dt} = \frac{X_{Kr}^{\infty} - X_{Kr}}{\tau_{Kr}}$$

$$R(V) = \frac{1}{1 + 2.5e^{.1(V+28)}}$$

$$\tau_{Kr} = 43 + \frac{1}{e^{-5.495+.1691V} + e^{-7.677-.0128V}}$$

$$X_{Kr}^{\infty} = \frac{1}{1 + e^{-2.182-.1819V}}$$

I_{Ks}

The slow delayed rectifier current was fit to data from Varro *et al*[10], specifically the results shown in figure 2 of their paper. The Winslow model was altered to increase the magnitude of the current and shift activation to less positive voltages.

$$I_{Ks} = \overline{G}_{Ks} X_{Ks}^2 (V - E_{Ks})$$

$$E_{Ks} = \frac{RT}{F} \ln\left(\frac{[K^+]_o + .01833[Na^+]_o}{[K^+]_i + .01833[Na^+]_i}\right)$$

$$\frac{dX_{Ks}}{dt} = \frac{X_{Ks}^{\infty} - X_{Ks}}{\tau_{Ks}}$$

$$X_{Ks}^{\infty} = \frac{1}{1 + e^{\frac{V-16}{-13.6}}}$$

$$\tau_{Ks} = \frac{1}{\frac{.0000719(V-10)}{1 - e^{-.148(V-10)}} + \frac{.000131(V-10)}{e^{.0687(V-10)} - 1}}$$

I_{to}

The transient outward current in the model is the same as in the Winslow model.

$$I_{to} = \bar{G}_{to} X_{to} Y_{to} (V - E_K)$$

$$\frac{dX_{to}}{dt} = \alpha_{Xto}(1 - X_{to}) - \beta_{Xto}$$

$$\frac{dY_{to}}{dt} = \alpha_{Yto}(1 - Y_{to}) - \beta_{Yto}$$

$$\alpha_{Xto} = .04516e^{.03577V}$$

$$\beta_{Xto} = .0989e^{-.06237V}$$

$$\alpha_{Yto} = \frac{.005415e^{\frac{V+33.5}{-5}}}{1 + .051335e^{\frac{V+33.5}{-5}}}$$

$$\beta_{Yto} = \frac{.005415e^{\frac{V+33.5}{5}}}{1 + .051335e^{\frac{V+33.5}{5}}}$$

I_{Kp}

The plateau potassium current is the same as in the Winslow model.

$$I_{Kp} = \bar{G}_{Kp} K_{Kp} (V - E_K)$$

$$K_{Kp} = \frac{1}{1 + e^{\frac{7.488 - V}{5.98}}}$$

I_{NaK}

The sodium-potassium pump current is the same as in the LRd model.

$$I_{NaK} = \bar{I}_{NaK} f_{NaK} \frac{1}{1 + (\frac{K_{mNai}}{[Na^+]_i})^{1.5}} \frac{[K^+]_o}{[K^+]_o + K_{mKo}}$$

$$f_{NaK} = \frac{1}{1 + .1245e^{\frac{-.1VF}{RT}} + .0365\sigma e^{\frac{-VF}{RT}}}$$

$$\sigma = \frac{1}{7}(e^{\frac{[Na^+]_o}{67.3}} - 1)$$

$I_{Nab}, I_{NaCa}, I_{pCa}, I_{Cab}$

$$I_{Nab} = \bar{G}_{Nab}(V - E_{Na})$$

The sodium-calcium exchange current, sarcolemmal pump current, and calcium and sodium background currents are the same as in the Winslow model.

$$I_{NaCa} = \frac{k_{NaCa}}{K_{mNa}^3 + [Na^+]_o^3} \frac{1}{K_{mCa} + [Ca^{2+}]_o} \frac{1}{1 + k_{sat} e^{\frac{VF(\eta-1)}{RT}}} (e^{\frac{VF\eta}{RT}} [Na^+]_i^3 [Ca^{2+}]_o - e^{\frac{VF(\eta-1)}{RT}} [Na^+]_o^3 [Ca^{2+}]_i)$$

$$I_{pCa} = \bar{I}_{pCa} \frac{[Ca^{2+}]_i}{K_{mpCa} + [Ca^{2+}]_i}$$

$$I_{Cab} = \overline{G}_{Cab}(V - E_{Ca})$$

$$E_{Ca} = \frac{RT}{2F} \ln(\frac{[Ca^{2+}]_o}{[Ca^{2+}]_i})$$

I_{Ca}

The L-type calcium current in the model is a modified version of that found in the LRd model. A time-dependent, enhanced Ca-induced inactivation was used, as well as a decrease in the current magnitude. These changes produced a smaller more rapidly inactivating calcium current, in agreement with experimental observations by Zygmunt (personal communication).

$$I_{Ca} = \bar{I}_{Ca} f df_{Ca}$$

$$\bar{I}_{Ca} = \frac{\overline{P}_{Ca}}{C_{sc}} \frac{4VF^2}{RT} \frac{[Ca^{2+}]_i e^{\frac{2VF}{RT}} - .341[Ca^{2+}]_o}{e^{\frac{2VF}{RT}} - 1}$$

$$\frac{df}{dt} = \frac{f^\infty - f}{\tau_f}$$

$$\frac{dd}{dt} = \frac{d^\infty - d}{\tau_d}$$

$$\frac{df_{Ca}}{dt} = \frac{f_{Ca}^\infty - f_{Ca}}{\tau_{fca}}$$

$$f^\infty = \frac{1}{1 + e^{\frac{V+12.5}{5}}}$$

$$\tau_f = 30 + \frac{200}{1 + e^{\frac{V+20}{9.5}}}$$

$$d^\infty = \frac{1}{1 + e^{\frac{V+10}{-6.24}}}$$

$$\tau_d = \frac{1}{\frac{.25e^{-.01V}}{1 + e^{-.07V}} + \frac{.07e^{-.05(V+40)}}{1 + e^{.05(V+40)}}}$$

$$f_{Ca}^\infty = \frac{1}{1 + (\frac{[Ca^{2+}]_i}{K_{mfca}})^3}$$

$$\tau_{fca} = 30$$

I_{CaK}

The potassium current through the L-type calcium channel is also a modified version of the LRd formulation.

$$I_{CaK} = \frac{\overline{P}_{CaK}}{C_{sc}} \frac{fdf_{Ca}}{1 + \frac{\bar{I}_{Ca}}{I_{Cahalf}}} \frac{1000VF^2}{RT} \frac{[K^+]_i e^{\frac{VF}{RT}} - [K^+]_o}{e^{\frac{VF}{RT}} - 1}$$

Ca handling

A modified form of the intracellular calcium dynamics from Chudin *et al*[4] was used. We included buffering from calmodulin in the cytoplasm and calsequestrin in the sarcoplasmic reticulum (SR), omitted spontaneous release of calcium from the SR, and combined the concentrations of calcium in the junctional sarcoplasmic reticulum (JSR) and the non-junctional sarcoplasmic reticulum (NSR) into a single variable.

$$\frac{d[Ca^{2+}]_i}{dt} = \beta_i (J_{rel} + J_{leak} - J_{up} - \frac{A_{Cap} C_{sc}}{2FV_{myo}} (I_{Ca} + I_{Cab} + I_{pCa} - 2I_{NaCa})$$

$$\beta_i = (1 + \frac{[CMDN]_{tot} K_m^{CMDN}}{(K_m^{CMDN} + [Ca^{2+}]_i)^2})^{-1}$$

$$J_{rel} = \overline{P}_{rel} fdf_{Ca} \frac{\gamma [Ca^{2+}]_{sr} - [Ca^{2+}]_i}{1 + 1.65 e^{\frac{V}{20}}}$$

$$\gamma = \frac{1}{1 + (\frac{2000}{[Ca^{2+}]_{sr}})^3}$$

$$J_{up} = \frac{V_{up}}{1 + (\frac{K_{mup}}{[Ca^{2+}]_i})^2}$$

$$J_{leak} = \overline{P}_{leak} ([Ca^{2+}]_{sr} - [Ca^{2+}]_i)$$

$$\frac{d[Ca^{2+}]_{sr}}{dt} = \beta_{sr} (J_{up} - J_{leak} - J_{rel}) \frac{V_{myo}}{V_{sr}}$$

$$\beta_{sr} = (1 + \frac{[CSQN]_{tot} K_m^{CSQN}}{(K_m^{CSQN} + [Ca^{2+}]_{sr})^2})^{-1}$$

Numerical Methods

The equations listed above were solved using parameter values and initial conditions found below. The simulations were run on Macintosh G3 and G4 computers using a program written in C. The numerical integration scheme was similar to that used in Luo and Rudy[1,2] and in Rush and Larsen[11]. Briefly, the time steps of integration were made small enough so that the changes in voltage and in calcium concentrations remained below maximum values, ΔV_{max} and ΔCa_{max}. If the changes in voltage and calcium concentration were below a minimum value (ΔV_{min} and ΔCa_{min}), the time step was increased. By keeping the changes in voltage small, we could solve the linear gate variable equations exactly during each time step. We used ΔV_{max} = .8 mV, ΔV_{min}=.2 mV, and ΔCa_{max}=1.067e-2 uM, ΔCa_{min}=2.67e-3 uM. The other time dependent variables in the model were solved using an adaptive fourth order Runge-Kutta method[12]. The errors were normalized as described in Jafri *et al*[13]. We used a maximum error of 1e-6, a minimum time step of .005 ms, and a maximum time step of .5 ms. During the stimulus, the step size was fixed at .005 ms. To further increase computational speed, lookup tables were used to avoid repeatedly calculating exponentials and other computationally expensive functions. The lookup tables were calculated once before each simulation for 15,000 values of voltages ranging from –100 mV to +100 mV. Values of voltages lying between the indices of the lookup table were calculated using linear interpolation.

Parameters:

$\overline{G}_{Na} = 12.8 \frac{mS}{\mu F}$

$\overline{G}_{K1} = 2.8 \frac{mS}{\mu F}$

$\overline{G}_{Kr} = .0136 \frac{mS}{\mu F}$

$\overline{G}_{Ks} = .0245 \frac{mS}{\mu F}$

$\overline{G}_{Kp} = .002216 \frac{mS}{\mu F}$

$\overline{G}_{to} = .23815 \frac{mS}{\mu F}$

$\overline{G}_{Na,b} = .0031 \frac{mS}{\mu F}$

$\overline{G}_{Ca,b} = .0003842 \frac{mS}{\mu F}$

$\overline{P}_{Ca} = .0000226 \frac{cm}{ms}$

$\overline{P}_{Ca,K} = 5.79 \times 10^{-7} \frac{cm}{ms}$

$\bar{I}_{Na,K} = .693 \frac{\mu A}{\mu F}$

$\bar{I}_{Cahalf} = -.265 \frac{\mu A}{\mu F}$

$K_{mfca} = .18 \frac{\mu mol}{L}$

$K_{mK1} = 13 \frac{mmol}{L}$

$K_{mNa} = 87.5 \frac{mmol}{L}$

$K_{mCa} = 1380 \frac{\mu mol}{L}$

$K_{mNai} = 10 \frac{mmol}{L}$

$K_{mKo} = 1.5 \frac{mmol}{L}$

$K_{mpCa} = .05 \frac{\mu mol}{L}$

$k_{NaCa} = 1500 \frac{\mu A}{\mu F}$

$k_{sat} = .2$

$\eta = .35$

$[Na^+]_i = 10 \frac{mmol}{L}$

$[K^+]_i = 149.4 \frac{mmol}{L}$

$A_{cap} = 1.534 \times 10^{-4} cm^2$

$V_{myo} = 25.84 \times 10^{-6} \mu L$

$V_{sr} = 2 \times 10^{-6} \mu L$

$V_{up} = .1 \frac{\mu M}{ms}$

$K_{mup} = .32 \mu M$

$\overline{P}_{rel} = 6 ms^{-1}$

$\overline{P}_{leak} = .000001 ms^{-1}$

$[CMDN]_{tot} = 10 \mu M$

$[CSQN]_{tot} = 10000 \mu M$

$K_m^{CMDN} = 2 \mu M$

$K_m^{CSQN} = 600 \mu M$

$C_{sc} = 1 \frac{\mu F}{cm^2}$

$R = 8.314 \frac{J}{molK}$

$T = 310 K$

$F = 96.5 \frac{coulomb}{mmol}$

$[K^+]_o = 4 \frac{mmol}{L}$

$[Na^+]_o = 138 \frac{mmol}{L}$

$[Ca^{2+}]_o = 2000 \frac{\mu mol}{L}$

Initial conditions:

$t = 0.0 ms$

$V = -94.7 mV$

$[Ca^{2+}]_i = .0472 \mu mol$

$[Ca^{2+}]_{sr} = 320 \mu mol$

$f = .983$

$d = .0001$

$m = 2.4676 \times 10^{-4}$

$h = .99869$

$j = .99887$

$fca = .942$

$xkr = .229$

$xks = .0001$

$xto = 3.742 \times 10^{-5}$

$yto = 1$

References

1. Luo CH, Rudy Y. A model of the ventricular cardiac action potential. *Circ Res*. 1991;68:1501-1526.

2. Luo CH, Rudy Y. A dynamic model of the cardiac ventricular action potential, I: simulation of ionic currents and concentration changes. *Circ Res*. 1994;74:1071-1096.

3. Winslow RL, Rice J, Jafri S, Marban E, O'Rourke B. Mechanisms of altered excitation-contraction coupling in canine tachycardia-induced heart failure, II. *Circ Res*. 1999;84:571-586.

4. Chudin E, Goldhaber J, Garfinkel A, Weiss J, Kogan B. Intracellular Ca^{2+} dynamics and the stability of ventricular tachycardia. *Biophys J*. 1999;77:2930-2941.

5. Liu DW, Antzelevitch C. Characteristics of the delayed rectifier current (I_{kr} and I_{ks}) in canine ventricular epicardial, midmyocardial, and endocardial myocytes. *Circ Res*. 1995;76:351-365.

6. Liu DW, Gintant GA, Antzelevitch C. Ionic bases for electrophysiological distinctions among epicardial, midmyocardial, and endocardial myocytes from the free wall of the canine left ventricle. *Circ Res*. 1993;72:671-687.

7. Zygmunt AC, Goodrow RJ, Antzelevitch C. I_{NaCa} contributes to electrical heterogeneity within the canine ventricle. *Am J Physiol*. 2000;278:H1671-H1678.

8. Freeman LC, Pacioretty LM, Moise NS Kass RS, Gilmour RF Jr. Decreased density of I_{to} in left ventricular myocytes from German shepherd dos with inherited arrhythmias. *J Cardiovasc Electrophysiol*. 1997;8:872-883.

9. Gintant GA. Characterization and functional consequences of delayed rectifier current transient in ventricular repolarization. *Am J Physiol*. 2000;278:H806-H817.

10. Varro A, Balati B, Iost N, Takacs J, Virag L, Lathrop DA, Csaba L, Talosi L, Papp JG. The role of the delayed rectifier component I_{Ks} in dog ventricular muscle and Purkinje fiber repolarisation. *J Physiol*. 2000;523.1:67-81.

11. Rush S, Larsen H. A particular algorithm for solving dynamics membrane equations. *IEEE Trans Biomed Eng*. 1978;25:389-392.

12. Press WH, Teukolsky SA, Vetterling WT, Flannery BP. *Numerical Recipes in C. Second edition*. Cambridge: Cambridge University Press, 1992.

13. Jafri S, Rice JJ, Winslow RL. Cardiac Ca^{2+} dynamics: the roles of ryanodine receptor adaptation and sarcoplasmic reticulum load. *Biophys J*. 1998;74:1149-1168.